Chemical
Science

ROYAL SOCIETY
OF CHEMISTRY

EDGE ARTICLE

View Article Online
View Journal

Cite this: DOI: 10.1039/d6sc00940a

All publication charges for this article have been paid for by the Royal Society of Chemistry

A novel lactam-based AIE building block for high-performance deep-blue electroluminescent materials

Luyao Liu,†[a] Jingli Lou,†[a] Jiaxing Wan,[a] Yin Li,[b] Hao Xiong,[a] Yu Huang,[a] Dezhi Yang,[a] Han Zhang,*[c] Ben Zhong Tang[d] and Zhiming Wang*[a]

Received 3rd February 2026
Accepted 30th March 2026

DOI: 10.1039/d6sc00940a

rsc.li/chemical-science

Developing high-performance deep-blue organic light-emitting diodes (OLEDs) requires the emitters to achieve a good balance among emission color, exciton utilization efficiency, and photoluminescence quantum yield (PLQY) in solid films. Herein, we report a new deep-blue emissive building block, abbreviated as PADP, which exhibits aggregation-induced emission (AIE) characteristics. Its solid-state emission peak is located at 408 nm, effectively filling a gap in AIE-based blue-emitting frameworks within this spectral region. Studies on substitution at the 6-position of PADP demonstrate that the introduction of strong electron-donating groups can effectively modulate the S_1 excited-state properties, promote the formation of hybridized local and charge-transfer (HLCT) states, and activate hot-exciton channels in the electroluminescence process to harvest high-lying triplet excitons. Among these derivatives, PADP-TPA with triphenylamine modification exhibits a maximum external quantum efficiency (EQE) of 9.2% in a deep-blue OLED with CIE coordinates of (0.154, 0.049), representing state-of-the-art performance for OLEDs based on deep-blue AIE fluorescent materials. These results not only elucidate the structure–property relationships of the PADP building block but also demonstrate its significant potential for the design of highly efficient deep-blue OLED emitters.

1. Introduction

Organic light-emitting diodes (OLEDs) are regarded as the most promising next-generation display and lighting technology due to numerous advantages such as low power consumption, high contrast ratio, and self-luminescence.[1] As one of the three primary colors, deep-blue light plays a crucial role in reducing the power consumption of displays.[2] However, constructing deep-blue organic emitters generally requires a balance between short conjugation length and high photoluminescence quantum yield (PLQY), which remains challenging.[3] Meanwhile, conventional deep-blue emissive building blocks typically adopt rigid planar structures and are therefore susceptible to aggregation-caused quenching (ACQ).[4] Consequently, the development of novel high-performance deep-blue emissive building blocks is particularly crucial, with aggregation-induced emission (AIE) offering an effective strategy to address this challenge.[5]

Fig. 1a presents the representative blue AIE building blocks. Among them, TPNS-H, TPE, TPPIO, and HPS exhibit emission peaks above 445 nm in the solid state.[6] Further structural modification of these molecules often induces a red shift in emission, causing deviation from the deep-blue region. In contrast, 1,2,4,5-TPB, PentaPP, and TPP display ultraviolet emission in the solid state while retaining AIE characteristics and have therefore been widely employed in the design and development of deep-blue electroluminescent (EL) materials.[7,8] In 2019, Zeng *et al.* reported a class of diphenylethene derivatives with AIE properties, among which SIP-2 achieved deep-blue emission peaking at 416 nm in the solid state; however, its EL performance has not yet been investigated.[9] Overall, AIE building blocks capable of deep-blue emission remain scarce, highlighting the urgent need for breakthroughs in molecular structure design.

Generally, multi-rotor structures may endow a material with AIE properties. On the one hand, the rotor units suppress close molecular packing, thereby preventing strong π–π interactions; on the other hand, restriction of intramolecular motion in the aggregated state inhibits nonradiative decay pathways, leading to enhanced emission.[10] In view of this, we found that

---

[a] *AIE Institute, State Key Laboratory of Luminescent Materials and Devices, Center for Aggregation-Induced Emission, South China University of Technology (SCUT), Guangzhou 510640, China. E-mail: wangzhiming@scut.edu.cn*

[b] *Jianghan University, Institute of Intelligent Sport and Proactive Health, School of Physical Education, Wuhan, 430056, China*

[c] *Department of Chemistry, Hong Kong Branch of Chinese National Engineering Research Center for Tissue Restoration and Reconstruction, The Hong Kong University of Science and Technology, Clear Water Bay, Kowloon, Hong Kong 999077, China. E-mail: cheungham@ust.hk*

[d] *Shenzhen Institute of Aggregate Science and Technology, School of Science and Engineering, The Chinese University of Hong Kong, Shenzhen 518172, China*

† These authors contributed equally to this work.

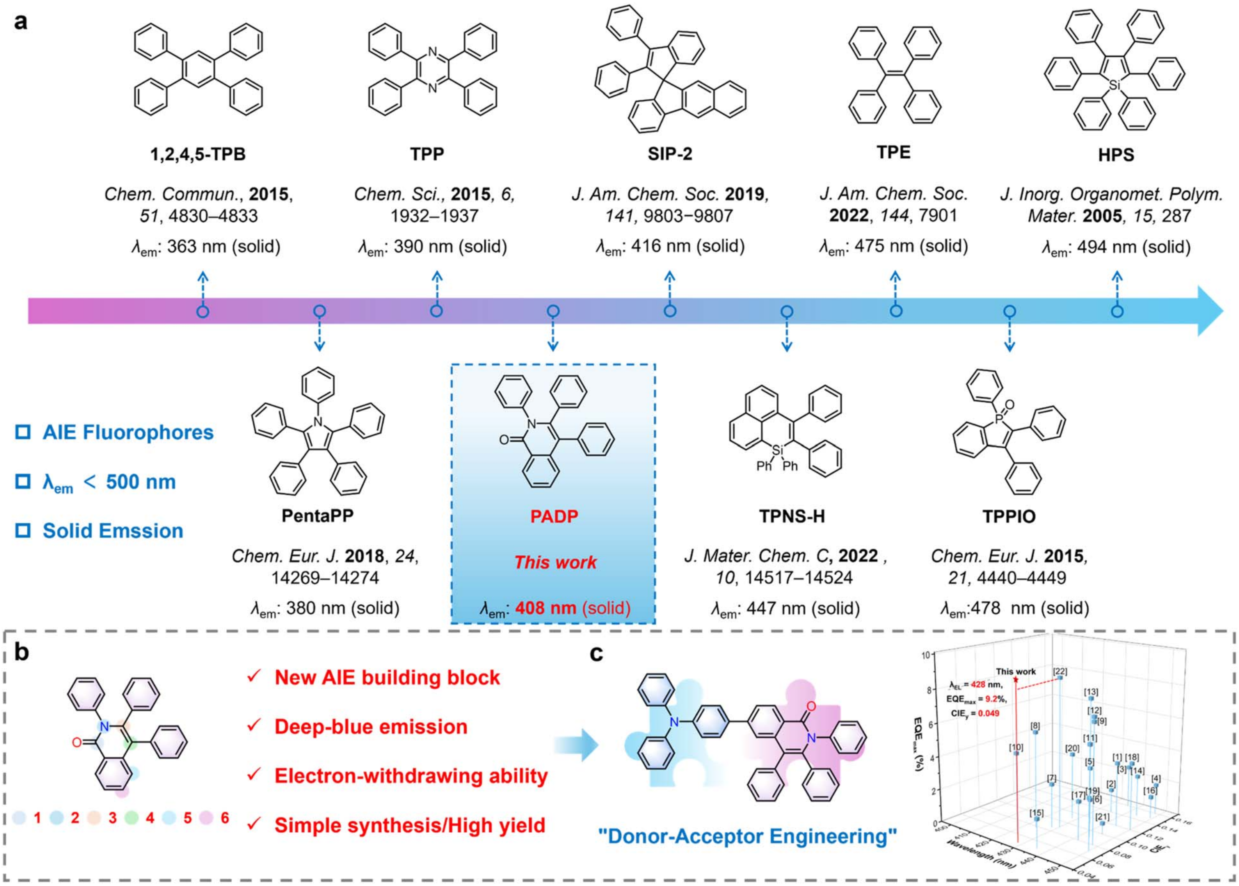

Fig. 1 (a) The main fluorescent molecules with AIE properties (λ_{em} < 500 nm). (b) Molecular PADP and the sequence of naming its sites. (c) Molecular PADP-TPA; and λ_{EL}-CIE$_y$-EQE$_m$ summary data of deep-blue ($\lambda_{EL} \leq 450$ nm) AIE fluorescent materials applied to OLEDs.

isocoumarin-based structures hold great potential for the development of AIE deep-blue chromophores.[11] The periphery can be modified with benzene rings to increase the number of rotors. Moreover, the incorporation of carbon-based components could reduce the electron injection barrier. Substitution of O atoms with N atoms not only enhances the intrinsic thermal stability of the material but also weakens its acceptor ability and increases the rotor count.

Herein, we design a novel building block PADP based on a multi-rotor lactam framework, which not only exhibits AIE properties but also achieves deep blue emission peaking at 408 nm in the solid state (Fig. 1a and b). Modifying the 6-position of PADP with an electron-donating group triphenylamine (TPA) not only significantly enhances its thermal stability and tunes the emission color but also endows it with excellent electroluminescent (EL) performance (Fig. 1c). In particular, the doped OLED based on PADP-TPA achieves deep blue emission at 428 nm, with a maximum EQE of 9.2% and CIE coordinates of (0.154, 0.049). PADP is demonstrated to be a promising blue-light building block, providing a solid foundation for the subsequent construction of more efficient materials. Moreover, this work verifies that the "lactam + multi-rotor" strategy offers valuable guidance for the development of high-performance deep-blue organic materials.

2. Results and discussion

2.1. Synthesis and characterization

As shown in Fig. 2, benzoic acid/4-bromobenzoic acid first undergoes a [4 + 2] cycloaddition reaction with 1,2-diphenylethyne to form 3,4-diphenyl-1*H*-isochromen-1-one/6-bromo-3,4-diphenyl-1*H*-isochromen-1-one (PADA/PADA-Br), using bis[(pentamethylcyclopentadienyl)dichloro-rhodium] as the catalyst and silver carbonate as the oxidant.[12] Then, after being treated with ammonium acetate in 110 °C dimethyl sulfoxide, 3,4-diphenylisoquinolin-1(2*H*)-one/6-bromo-2,3,4-triphenylisoquinolin-1(2*H*)-one (PADH/PADH-Br) can be efficiently obtained.[13] In the presence of copper as a catalyst, PADH/PADH-Br reacts with a hypervalent iodine salt (diphenyliodonium hexafluorophosphate) to generate the final product 2,3,4-triphenylisoquinolin-1(2*H*)-one (PADP) or the key intermediate 6-bromo-2,3,4-triphenylisoquinolin-1(2*H*)-one (PADP-Br).[14] Finally, the target compounds PADP-pCz, PADP-mCz, and PADP-TPA are obtained *via* Suzuki–Miyaura cross-coupling reactions of PADP-Br with the corresponding (4-(9*H*-carbazol-9-yl)phenyl)boronic acid, (3-(9*H*-carbazol-9-yl)phenyl) boronic acid, and (4-(diphenylamino)phenyl)boronic acid, respectively.[15] The detailed synthetic routes are outlined in

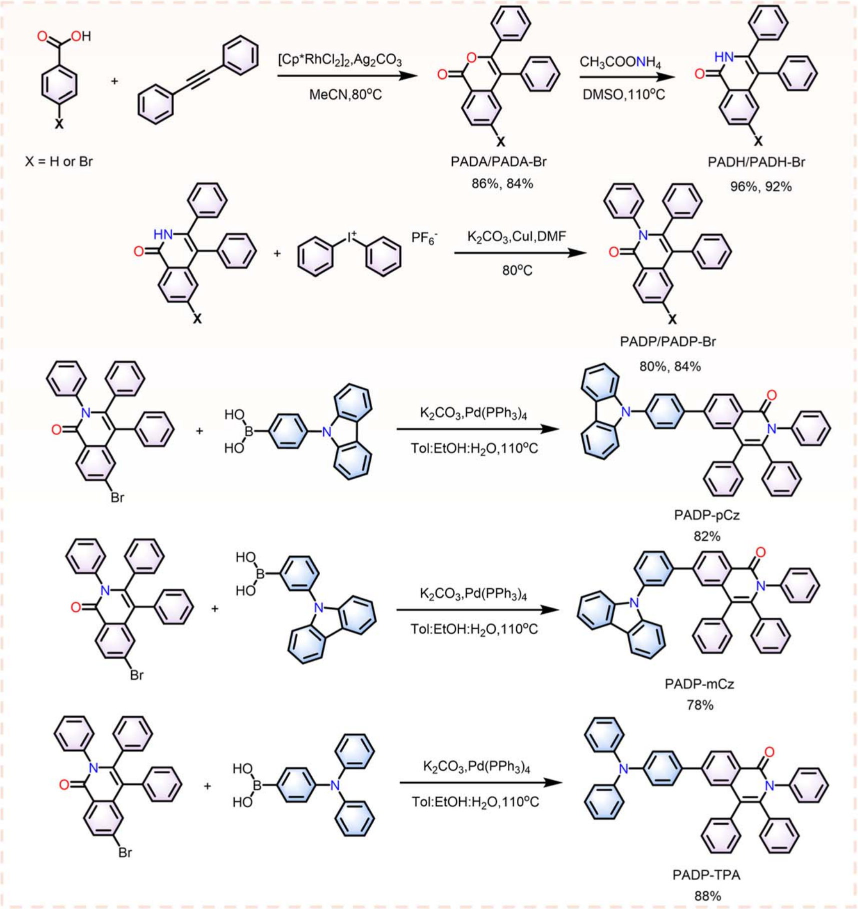

Fig. 2 Synthesis route and structure of PADP, PADP-pCz, PADP-mCz, and PADP-TPA.

Table 1 Optical, thermal, and electrochemical properties of PADP, PADP-pCz, PADP-mCz, and PADP-TPA

		λ_{PL} [nm]		$\eta_{\mathrm{PL}}{}^{c}$ [%]		τ [ns]				
Compound	$\lambda_{\mathrm{abs}}{}^{a}$ [nm]	Soln^{a}	Film^{b}	Soln^{a}	Film^{b}	Soln^{a}	Film^{b}	$S_1/T_1/\Delta E_{\mathrm{S1T1}}{}^{d}$ [eV]	T_g/T_d [°C]	$\mathrm{IP_{CV}/EA_{CV}}{}^{e}$ [eV]
PADP	304	395	408/—	3.7	8.8/—	0.71	—	3.50/2.64/0.86	266/—	5.75/2.22
PADP-pCz	293/316	423	422/—	6.4	7.5/—	1.00	—	3.28/2.63/0.65	410/143	5.33/2.46
PADP-mCz	282/340	423	417/—	5.4	7.5/—	0.97	—	3.26/2.63/0.63	402/135	5.34/2.45
PADP-TPA	308/358	420	447/428	69.6	65.7/81.0	1.75	2.29/2.18	3.17/2.61/0.56	344/158	5.26/2.35

[a] In toluene solution (10^{-5} M). [b] Film: the former refers to vacuum-deposited neat films, while the latter denotes vacuum-deposited doped films with PADP-TPA doped in the mCPBC host at a concentration of 20 wt%. [c] Fluorescence quantum yield, determined by using a calibrated integrating sphere. [d] Calculated from the emission spectra in solution, with S_1 obtained from fluorescence (room temperature) and T_1 from phosphorescence (77 K). [e] Determined by CV measurement in solutions.

Scheme S1. All the target products have been fully confirmed by $^{1}H/^{13}C$ NMR and high-resolution mass spectrometry (HRMS).

The thermal properties of the target compounds were evaluated by thermogravimetric analysis (TGA) and differential scanning calorimetry (DSC). The thermal decomposition temperatures (T_d) of PADP, PADP-pCz, PADP-mCz, and PADP-TPA were recorded as 266 °C, 410 °C, 402 °C, and 344 °C, respectively (Fig. S1 and Table 1), while the corresponding glass transition temperatures (T_g) were determined to be 143 °C, 135 °C, and 158 °C, respectively. In contrast, no obvious glass transition temperature was observed for PADP within the tested temperature range (Fig. S1 and Table 1). These data indicate that the increase in molecular weight enhances thermal stability, enabling the possibility of fabricating vapor-deposited devices. The energy levels of the highest occupied molecular orbital (HOMO) and the lowest unoccupied molecular orbital (LUMO) were approximated from the ionization potential (IP) and electron affinity (EA) of PADP, PADP-pCz, PADP-mCz, and PADP-TPA, which were estimated by cyclic voltammetry (Fig. S2), with values of −5.75 and −2.22 eV, −5.33 and −2.46

eV, −5.34 and −2.45 eV, and −5.26 and −2.35 eV, respectively (Table 1). The incorporation of donor moieties reduces the HOMO–LUMO gaps, thus facilitating efficient carrier injection. Single crystals of PADP, PADP-pCz, and PADP-mCz were obtained by slow *n*-hexane diffusion in dilute dichloromethane solutions (Fig. S3–S5). Crystal structure analysis reveals that the torsion angles of the three peripheral phenyl ring rotors fall in the range of 68.28–87.77°, thereby exerting an inhibitory effect on molecular packing.[16] The slipped π–π stacking observed in PADP-mCz, with an intermolecular π–π distance of approximately 3.921 Å, further supports this conclusion. The presence of carbonyl groups gives rise to extensive intermolecular C–H⋯O interactions, which could stabilize the molecular conformation and suppress vibrational relaxation, ultimately leading to high PLQY.[17]

2.2. Theoretical calculation

Density functional theory (DFT) and time-dependent density functional theory (TD-DFT) calculations were performed to investigate the electronic structures and energy levels of PADP, PADP-pCz, PADP-mCz and PADP-TPA.[18] As shown in Fig. 3b, the HOMO of PADP is mainly distributed on two fused six-membered rings and the peripheral benzene ring rotors at the 2- and 3-positions, whereas the LUMO is distributed on two fused six-membered rings and the carbonyl group. Following modification of the donor moiety, the HOMOs of PADP derivatives are primarily localized on the donor segments. However, a portion of the HOMO in PADP-TPA is delocalized onto the acceptor moiety of the PADP framework. The LUMOs of the three PADP derivatives are all distributed over the two fused six-membered rings, the carbonyl groups, and the benzene rings attached to the PADP acceptors.

Fig. 3c shows the energy level distributions of PADP, PADP-pCz, PADP-mCz, and PADP-TPA. Large energy gaps (ΔE_{ST}) between the lowest singlet state (S_1) and the lowest triplet state (T_1) are observed, with values of 1.18, 0.87, 0.89, and 0.85 eV, respectively, indicating that the reverse intersystem crossing (RISC) from T_1 to S_1 is significantly hindered. Natural transition orbital (NTO) analysis reveals that the S_1 states of all four molecules exhibit hybridized local and charge-transfer (HLCT) character, arising from the admixture of local excitation (LE) and charge-transfer (CT) contributions (Tables S8–S11). For PADP, the energy gap between the T_2 and S_1 is calculated to be 0.2 eV. Although this transition is endothermic and non-spontaneous, the small energy discrepancy below 0.3 eV renders the high-lying RISC process possible. According to Fermi's golden rule, the spin–orbit coupling (SOC) is another driving force for the occurrence of RISC.[19] The calculated SOC matrix element

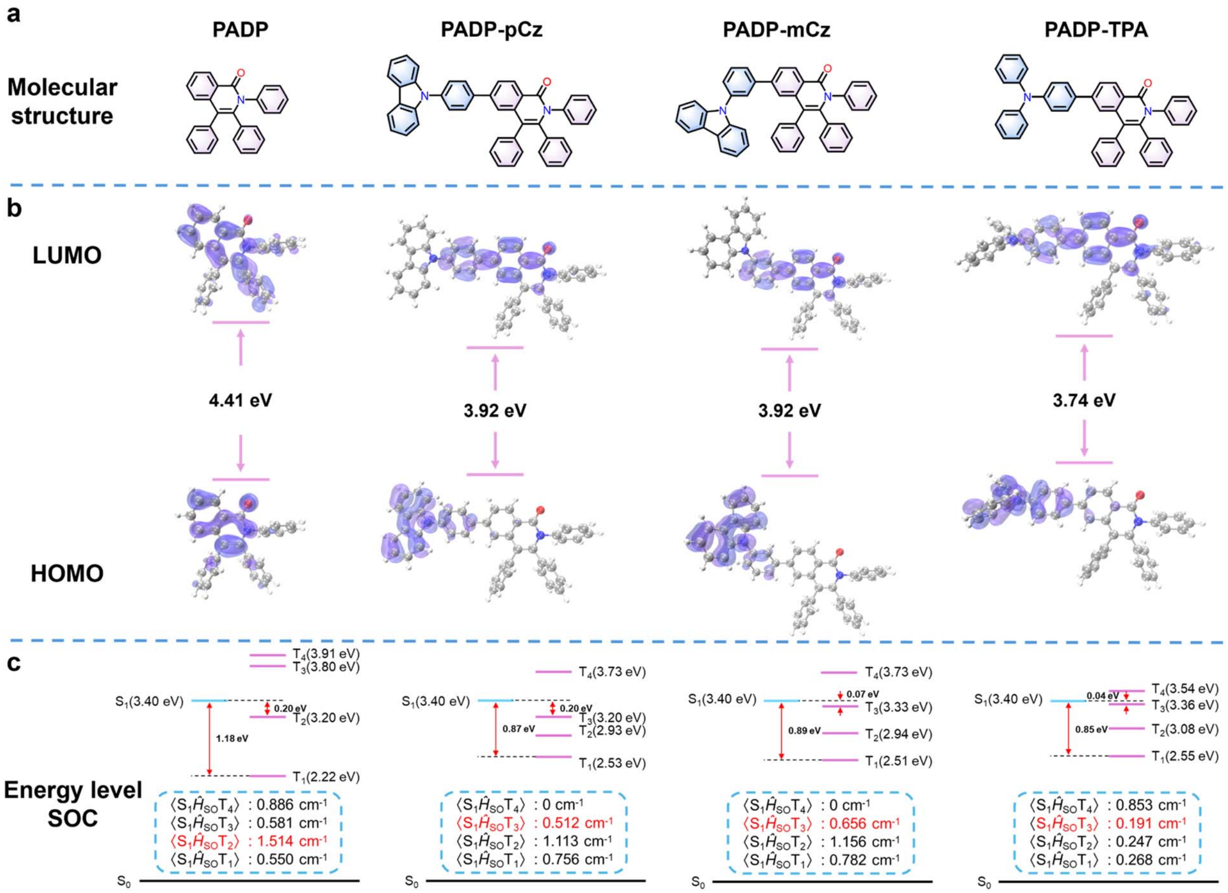

Fig. 3 (a) Molecule structures. (b) Frontier orbital distributions. (c) Singlet and triplet energy levels and SOC matrix elements of PADP, PADP-pCz, PADP-mCz, and PADP-TPA.

$\langle S_1|\hat{H}_{\mathrm{SOC}}|T_2\rangle$ of PADP is as large as 1.514 cm^{-1}, which provides an additional driving force for the $T_2 \rightarrow S_1$ transition. For triplet states lying above the S_1 level (*e.g.* T_3 and T_4), the corresponding RISC processes are spontaneous and exothermic and can likewise be activated, with SOC facilitating the process. Analogous energy distributions are observed in PADP-pCz, PADP-mCz and PADP-TPA, indicating that similar hRISC channels might also exist in these three materials.

2.3. Photophysical properties

The ultraviolet-visible (UV-vis) absorption spectra of PADP, PADP-pCz, PADP-mCz, and PADP-TPA in toluene solutions (10^{-5} M) are depicted in Fig. 4a. The absorption bands below 310 nm are caused by the π–π* transitions of PADP, 9-phenylcarbazole, and triphenylamine segements, while the absorption above 310 nm results from the extended *π*-conjugation between the donor and PADP (Table 1).[20] PADP, PADP-pCz, PADP-mCz, and PADP-TPA show emission peaks at 395, 423, 423, and 420 nm in toluene solution, with a corresponding PLQY of 3.7%, 6.4%, 5.4%, and 69.6%, respectively (Fig. 4a and Table 1). The significant increase in the PLQY of PADP-TPA is primarily due to its S_1 state exhibiting a more pronounced overlap of electron and hole distributions than those of the other three molecules (Tables S8–S11). To investigate the excited states, absorption spectra and PL spectra in solvents with different polarities were measured (Fig. S6, S7, and Tables S12–S15). As the solvent polarity increases, the PL spectra of these emitters gradually red-shift and broaden, accompanied by the disappearance of the fine vibrational structure, which implies a change in the excited state. The Lippert–Mataga plot reveals the relationship between the Stokes shift ($\nu_a - \nu_f$) and the solvent orientational polarizability (*f*) (Fig. 4b; eqn (S1) and (S2)).[21] Among them, PADP, PADP-pCz, and PADP-mCz exhibit two segments of linear relationships. In low-polarity solvents ($f \leq 0.167$), their excited-state dipole moments (μ_e) are 6.80, 9.41, and 8.55 D, respectively, corresponding to a LE state originating from the PADP core moiety. In high-polarity solvents ($f \geq 0.210$), the corresponding values increase to 12.34, 13.16, and 12.68 D, which can be attributed to the CT state descending to become the dominant excited state. In contrast, PADP-TPA exhibits a single-slope fitting across the entire range of polar solvents, with the dipole moment of the S_1 state estimated to be 15.56 D. This μ_e value is higher than that of conventional LE-state molecules (8 D) while lower than that of typical CT-state molecules (*e.g.*, DMABN, μ_e = 23 D),[22] which confirms the quasi-equivalent hybridization between the LE and CT components. These results indicate that when the donor strength is sufficiently high, it can influence the S_1 state, thereby affecting its luminescence.

The emission peaks of the vacuum-deposited neat films of the four molecules are redshifted to 408, 422, 417, and 447 nm, respectively (Table 1 and Fig. S8). Among them, PADP-TPA exhibits the largest redshift, which may originate from strong intermolecular interactions.[23] The PLQYs of PADP, PADP-pCz, PADP-mCz, and PADP-TPA in neat films are 8.8%, 7.5%, 7.5%, and 65.7%, respectively (Table 1). When PADP-TPA is doped into a low-polarity mCPBC host at a concentration of 20 wt%, the vacuum-deposited doped film exhibits a reduced redshift and achieves deep-blue emission at 428 nm (Fig. S9), with a corresponding QY value of 81.0%. The PL changes in the molecules in THF/water mixed systems were further investigated. PADP, PADP-pCz, and PADP-mCz exhibit typical AIE or AEE behavior, and their PL intensities reach maximum values when the water fraction increases to 99, 70, and 80%, respectively (Fig. 4c and S10). For PADP-TPA, it shows a twisted intramolecular CT characteristic when the water fraction is below 60%; when the water fraction exceeds 60%, pronounced molecular aggregation occurs, leading to an aggregation-induced blue shift and enhanced emission. The S_1 and T_1 energy levels were estimated from the room-temperature

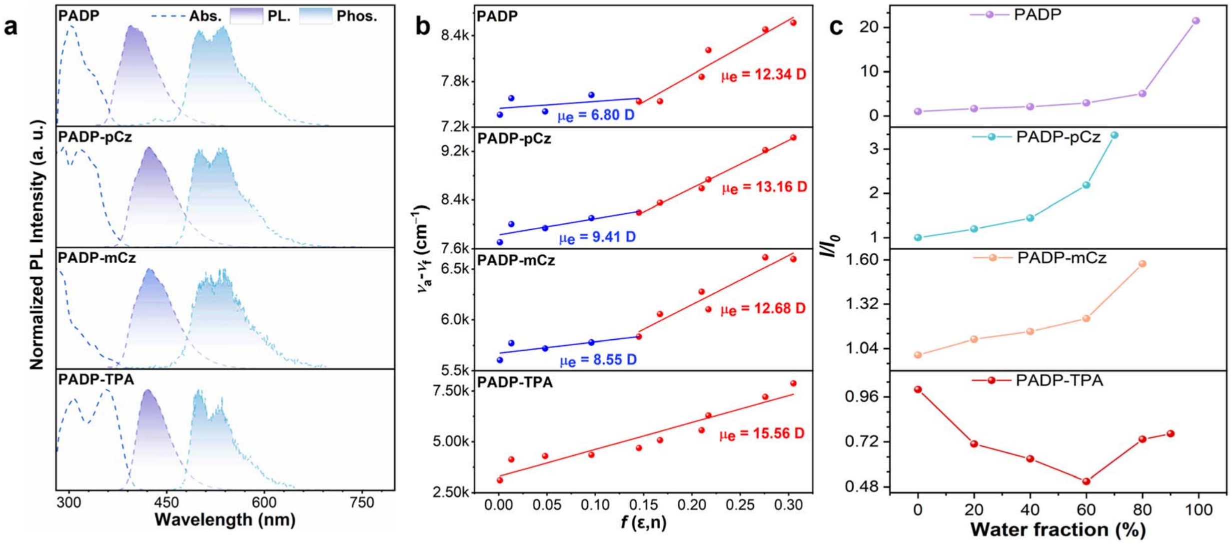

Fig. 4 (a) UV-vis absorption and fluorescence spectra in 10^{-5} M toluene at room temperature and phosphorescence spectra in toluene at 77 K. (b) The Lippert–Mataga plots. (c) The graph showing the relationship between I/I_0 and f_w for PADP, PADP-pCz, PADP-mCz, and PADP-TPA; where I_0 is the PL intensity in pure THF solution.

fluorescence spectra and 77 K phosphorescence spectra (Fig. 4a), yielding ΔE_{ST} values of 0.86, 0.65, 0.62, and 0.56 eV for the four molecules (Table 1), respectively. The large energy gaps (>0.3 eV) are unfavorable for the RISC process, making the occurrence of TADF rather difficult.[24] The lifetimes of PADP, PADP-pCz, PADP-mCz, and PADP-TPA in solution, as well as of PADP-TPA in the film, show a single-exponential decay on the nanosecond timescale, which further rules out the possibility of these materials as TADF emitters (Fig. S11).[25]

2.4. Electroluminescence properties

To evaluate the potential of these new molecules for EL applications, they were employed as the emissive layer (EML) in OLEDs. The optimized structure of the nondoped device is ITO (90 nm)/HATCN (5 nm)/TAPC (50 nm)/TCTA (5 nm)/EML (20 nm)/TmPyPB (50 nm)/LiF (1 nm)/Al (120 nm), where the EMLs are PADP-pCz, PADP-mCz, and PADP-TPA, respectively. In these devices, ITO (indium tin oxide) and aluminum are adopted as the anode and cathodes, respectively; 1,4,5,8,9,11-hexaazatriphenylenehexacarbonitrile (HATCN) is a well-known hole-injecting material; di-(4-(*N*,*N*-ditolyl-amino)-phenyl)cyclohexane (TAPC) works as a hole-transporting layer; tris(4-carbazoyl-9-ylphenyl)amine (TCTA) serves as an exciton-blocking layer; 3,3′-[5′-[3-(3-Pyridinyl)phenyl][1,1′:3′,1″-terphenyl]−3,3″-diyl]bispyridine (TmPyPB) and lithium fluoride (LiF) function as the electron transfer layer (ETL) and electron-injection layer. The performances of these non-doped OLEDs are summarized in Table 2. The EL spectra of PADP-pCz, PADP-mCz, and PADP-TPA exhibit deep-blue emissions at 424, 426, and 442 nm, which are consistent with their PL spectra in neat films (Fig. S8 and S12). The devices based on PADP-pCz, PADP-mCz, and PADP-TPA exhibit maximum luminances of 1246, 1046, and 8635 cd m^{-2}, respectively, with corresponding CIE coordinates of (0.155, 0.079), (0.157, 0.083), and (0.149, 0.072) (Table 2 and Fig. S12). The maximum EQEs of these devices are 0.4%, 0.5%, and 6.7%, respectively. The EL performances of PADP-pCz and PADP-mCz are limited, primarily due to their relatively low PLQYs. In contrast, PADP-TPA exhibits superior EL performance, indicating promising application potential.

Doped OLEDs based on PADP-TPA were further fabricated using mCPBC as the low-polarity host. Meanwhile, 2Na-CzCN was introduced as the exciton enhancement layer (EEL),[26] and the ETL was changed from TmPyPB to bathophenanthroline (BPhen). The optimized device structure is as follows: ITO (90 nm)/HATCN (5 nm)/TAPC (50 nm)/TCTA (5 nm)/EML (16 nm)/AMI (5 nm)/BPhen (50 nm)/LiF (1 nm)/Al (120 nm) (Fig. 5a and b). The doped device exhibits a low turn-on voltage of 3.0 V and achieves deep-blue emission at 428 nm, with the luminance increased from 8635 cd m^{-2} (non-doped device) to 10 280 cd m^{-2} (Table 2 and Fig. 5e). Additionally, the maximum EQE of the doped device reaches 9.2% (Fig. 5f), maintaining an EQE of 8.3% at 1000 cd m^{-2} with a small efficiency roll-off of 9.8%, and corresponding color coordinates of (0.154, 0.049). The CIE$_y$ value is close to the Broadcast Service Television 2020 (BT.2020) blue standard (Table 2 and Fig. 5d).[27] To the best of our knowledge, this represents a state-of-the-art performance for deep-blue AIE fluorescent materials reported so far ($\lambda_{\text{EL}} \leq 450$ nm) (Fig. 1c and Table S17).

To further investigate the EL mechanism in the doped and non-doped devices, the main parameters affecting EL efficiency are discussed in accordance with the corresponding formula (eqn (1)):[28]

$$\eta_{\text{ext}} = \gamma \eta_{\text{PL}} \eta_{\text{r}} \eta_{\text{out}} \tag{1}$$

Among these parameters, η_{ext} refers to the EQE, γ is the electron–hole recombination efficiency (theoretically up to 100%), η_{PL} denotes the PLQY of vacuum-deposited films, η_{r} represents the radiative exciton utilization efficiency, and η_{out} stands for the light outcoupling efficiency (Table S18). Angle-dependent PL measurements illustrate that both the neat film and the doped film of PADP-TPA exhibit excellent horizontal dipole orientation ratios ($\Theta\|$) of 91.0% and 90.0%, respectively (Fig. 5c). In contrast, the $\Theta\|$ values of PADP-pCz and PADP-mCz neat films are as low as 73.5% and 64.5% (Fig. S13). Further optical simulations were performed based on the device structures,[29] yielding η_{out} values of 36.4% and 35.6% for PADP-TPA in the neat film and doped film, respectively, and 27.6% and 25.2% for PADP-pCz and PADP-mCz in their neat films, respectively (Table S18). Combined with eqn (1), the theoretical maximum EQEs of the nondoped devices based on PADP-pCz, PADP-mCz, and PADP-TPA and doped device based on PADP-TPA are calculated to be 0.5%, 0.5%, 6.0%, and 7.7% respectively. However, the experimentally measured values are 0.4%, 0.5%, 6.7%, and 9.2%, respectively. The theoretical and experimental efficiencies of the PADP-pCz and PADP-mCz-based devices are in good agreement, indicating that they behave as conventional fluorescent materials. In contrast, both nondoped and doped devices based on PADP-TPA exhibit efficiencies that significantly exceed their theoretical limits, suggesting that the exciton utilization efficiency surpasses the 25% limit of conventional fluorescent

Table 2 Summary of performance devices.

Emitters	$\lambda_{\text{EL}}{}^{a}$ (nm)	$V_{\text{on}}{}^{b}$ (V)	L^{c} (cd m^{-2})	$\eta_{\text{C}}{}^{c}$ (cd A^{-1})	$\eta_{\text{P}}{}^{c}$ (lm W^{-1})	EQE$_{\text{max}}$/EQE@1000 cd m^{-2d} (%)	CIE^{e} (x, y)	FWHM^{a}
PADP-pCz	424	3.4	1246	0.24	0.22	0.4/0.4	0.155, 0.079	82
PADP-mCz	426	4.2	1046	0.28	0.21	0.5/0.4	0.157, 0.083	78
PADP-TPA	442	3.0	8635	4.26	4.38	6.7/6.0	0.149, 0.072	60
20 wt.% PADP-TPA	428	3.0	10 280	3.56	3.44	9.2/8.3	0.154, 0.049	56

[a] EL maximum emission peak. [b] Turn-on voltage at 1 cd m^{-2}. [c] L = maximum luminance, η_{C} = maximum current efficiency, and η_{P} = maximum power efficiency. [d] Maximum external quantum efficiency/external quantum efficiency at 1000 mA cm^{-2}. [e] CIE.

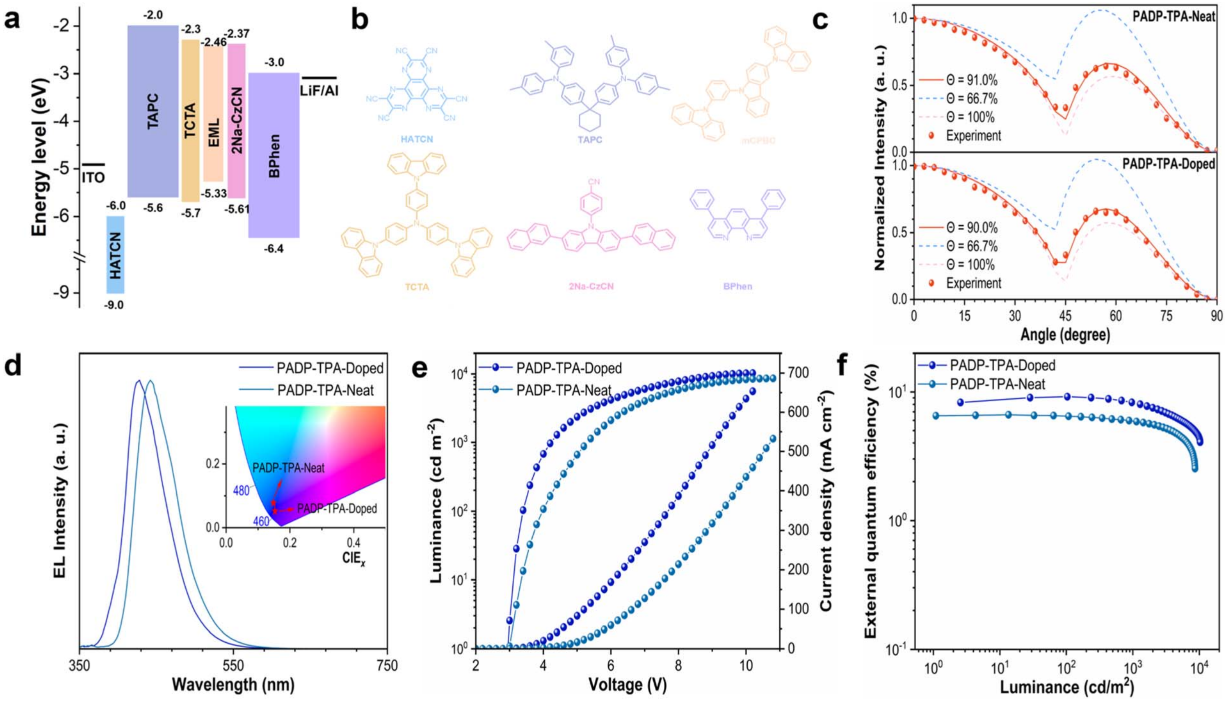

Fig. 5 (a) Doped device structure; (b) structure of the functional layers; (c) measured horizontal transition dipole moment ratios of PADP-TPA in the neat film and doped film. (d) PADP-TPA pure film EL spectrum and EL spectrum of the device with 20 wt% PADP-TPA doped in the mCPBC host; the inset shows the CIE coordinates of the EL spectra. (e) Current density–voltage–luminance characteristics of the devices. (f) The external quantum efficiency *versus* the current density.

materials.[30] Therefore, RISC processes from higher-lying triplet states to the singlet state, as explained by theoretical calculations, are likely operative for PADP-TPA. From the current density–luminance curves, a linear relationship is observed for both PADP-TPA-based nondoped and doped devices, which further rules out the involvement of triplet–triplet annihilation (TTA) (Fig. S14). Consequently, a "hot exciton" mechanism is confirmed for PADP-TPA. These findings further corroborate that the introduction of a strong donor in this system can substantially modulate the luminescence performance.

3. Conclusion

In summary, we have developed a rare deep-blue-emitting lactam building block PADP with AIE properties, which exhibits deep-blue emission at 408 nm in the solid state. Donor modification at the 6-position of PADP not only enhances the thermal stability, but also promotes the formation of HLCT states when the donor strength reaches a sufficient level. Compared with pCz and mCz units, PADP-TPA modified with the stronger electron-donating TPA unit exhibits quasi-equivalent hybridization between the LE and CT components, resulting in significantly enhanced PLQY and EL performance relative to PADP-pCz and PADP-mCz. Meanwhile, PADP-TPA exhibits a horizontal dipole orientation exceeding 90% in solid-state films and can harvest high-lying triplet states *via* a hot-exciton mechanism during the EL process. The corresponding doped deep-blue OLED achieves a record-high EQE of 9.2% with CIE coordinates of (0.154, 0.049). This work demonstrates that the "lactam + multi-rotor" design provides valuable guidance for the development of a blue AIE building block and offers insights for the future design of advanced deep-blue electroluminescent materials.

Author contributions

L. Liu synthesized the emitters. J. Lou fabricated and characterized the OLED devices. L. Liu, J. Wan, Y. Li, H. Xiong, and Y. Huang characterized the photophysical properties. L. Liu and H. Zhang wrote the manuscript. H. Zhang provided suggestions on experiments. D. Yang provided test support. Z. Wang and B. Z. Tang supervised and directed this study.

Conflicts of interest

There are no conflicts to declare.

Data availability

All data supporting this study are available in the supplementary information (SI). Additional data are available from the corresponding author upon reasonable request. Supplementary information is available. See DOI: https://doi.org/10.1039/d6sc00940a.

Acknowledgements

We are grateful for financial support from the National Natural Science Foundation of China (52473173 and U25A20569), Natural Science Foundation of Guangdong Province

(2022B1515020084), Guangdong Basic and Applied Basic Research Foundation (2023B1515040003), Key Project of Yunnan Provincial Department of Science and Technology (202303AC100021), Independent Research Project of State Key Lab of Luminescent Materials and Devices (SCUT) (Skllmd-2024-10,Skllmd-2025-05), Science and Technology Program of Guangzhou (2023A04J0988), Key-Area Research and Development Program of Guangdong Province (2024B0101040001), and the Innovation and Technology Commission (ITC-CNERC14SC01). We gratefully acknowledge HZWTECH for providing computation facilities.

References

1 (*a*) C. W. Tang and S. A. VanSlyke, *Appl. Phys. Lett.*, 1987, **51**, 913; (*b*) M. A. Baldo, D. F. O'Brien, Y. You, A. Shoustikov, S. Sibley, M. E. Thompson and S. R. Forrest, *Nature*, 1998, **395**, 151; (*c*) H. Uoyama, K. Goushi, K. Shizu, H. Nomura and C. Adachi, *Nature*, 2012, **492**, 234; (*d*) X. Ai, E. W. Evans, S. Dong, A. J. Gillett, H. Guo, Y. Chen, T. J. H. Hele, R. H. Friend and F. Li, *Nature*, 2018, **563**, 536; (*e*) Y. Xu, X. Liang, X. Zhou, P. Yuan, J. Zhou, C. Wang, B. Li, D. Hu, X. Qiao, X. Jiang, L. Liu, S.-J. Su, D. Ma and Y. Ma, *Adv. Mater.*, 2019, **31**, 1807388.

2 (*a*) Y. Sun, N. C. Giebink, H. Kanno, B. Ma, M. E. Thompson and S. R. Forrest, *Nature*, 2006, **440**, 908; (*b*) M. Mamada, A. Aoyama, R. Uchida, J. Ochi, S. Oda, Y. Kondo, M. Kondo and T. Hatakeyama, *Adv. Mater.*, 2024, **36**, 2402905.

3 J. Lou, G. Li, X. Guo, B. Li, D. Yang, H. Zhang, Z. Wang and B. Z. Tang, *Small*, 2024, **20**, 2308468.

4 (*a*) S. Rana, S. R. Nayak, S. Patel and S. Vaidyanathan, *J. Mater. Chem. C*, 2024, **12**, 765–818; (*b*) Y. Liu, C. Li, Z. Ren, S. Yan and M. R. Bryce, *Nat. Rev. Mater.*, 2018, **3**, 18020.

5 (*a*) J. Zhao, Z. Feng, D. Zhong, X. Yang, Y. Wu, G. Zhou and Z. Wu, *Chem. Mater.*, 2018, **30**, 929; (*b*) W. Yang, Y. Yang, L. Zhan, K. Zheng, Z. Chen, X. Zeng, S. Gong and C. Yang, *Chem. Eng. J.*, 2020, **390**, 124626.

6 (*a*) H. Wang, W. Feng, G. Gong, H. Chen, X. He, B. Li, T. Zhang, Z. Zhao, Z. Wang and B. Z. Tang, *J. Mater. Chem. C*, 2022, **10**, 14517; (*b*) J. Liu, H. Zhang, L. Hu, J. Wang, J. W. Y. Lam, L. Blancafort and B. Z. Tang, *J. Am. Chem. Soc.*, 2022, **144**, 7901–7910; (*c*) F. Bu, E. Wang, Q. Peng, R. Hu, A. Qin, Z. Zhao and B. Z. Tang, *Chem.–Eur. J.*, 2015, **21**, 4440–4449; (*d*) Y. Dong, J. W. Y. Lam, Z. Li, A. Qin, H. Tong, Y. Dong, X. Feng, B. Z. Tang and J. Inorg, *Organomet. Polym.*, 2005, **15**, 287–29.

7 L. Li, M. Chen, H. Zhang, H. Nie, J. Z. Sun, A. Qin and B. Z. Tang, *Chem. Commun.*, 2015, **51**, 4830–4833.

8 (*a*) Y. Lei, Q. Liu, L. Dong, Z. Cai, J. Shi, J. Zhi, B. Tong and Y. Dong, *Chem.–Eur. J.*, 2018, **24**, 14269–14274; (*b*) M. Chen, L. Li, H. Nie, J. Tong, L. Yan, B. Xu, J. Z. Sun, W. Tian, Z. Zhao, A. Qin and B. Z. Tang, *Chem. Sci.*, 2015, **6**, 1932–1937.

9 Z. Zhou, S. Xie, X. Chen, Y. Tu, J. Xiang, J. Wang, Z. He, Z. Zeng and B. Z. Tang, *J. Am. Chem. Soc.*, 2019, **141**, 9803–9807.

10 Y. Hong, J. W. Lam and B. Z. Tang, *Chem. Soc. Rev.*, 2011, **40**, 5361–5388.

11 R. Nazir, A. J. Stasyuk and D. T. Gryko, *J. Org. Chem.*, 2016, **81**, 11104–11114.

12 (*a*) T. Satoh and M. Miura, *Chemistry*, 2010, **16**, 11212–11222; (*b*) E. Kudo, Y. Shibata, M. Yamazaki, K. Masutomi, Y. Miyauchi, M. Fukui, H. Sugiyama, H. Uekusa, T. Satoh, M. Miura and K. Tanaka, *Chemistry*, 2016, **22**, 14190–14194; (*c*) X.-G. Liu, H. Gao, S.-S. Zhang, Q. Li and H. Wang, *ACS Catal.*, 2017, **7**, 5078–5086; (*d*) F. Yin, W. Peng, C. Wang, L. Qu, X. Chen, L. Kong and X. Wang, *Asian J. Org. Chem.*, 2022, **11**, e202200024.

13 V. B. Kharitonov, M. A. Arsenov, A. A. Danshina and D. A. Loginov, *INEOS OPEN*, 2023, **6**, 10–15.

14 M. E. Baumert, V. Le, P.-H. Su, Y. Akae, D. Bresser, P. Théato and M. M. Hansmann, *J. Am. Chem. Soc.*, 2023, **145**, 23334–23345.

15 (*a*) H. Zhang, J. Lou, K. Zhang, X. Guo, G. Li, B. Li, B. Ma, C. Xiao, L. Liu, Y. Chen, D. Yang, D. Ma, J. Sun, J. W. Y. Lam, Z. Wang and B. Z. Tang, *Adv. Mater.*, 2025, **37**, 2419217; (*b*) B. Ma, B. Zhang, H. Zhang, Y. Huang, L. Liu, B. Wang, D. Yang, D. Ma, B. Z. Tang and Z. Wang, *Adv. Sci.*, 2024, **11**, 2407254.

16 B. Li, J. Lou, H. Zhang, G. Li, X. He, Y. Huang, N. Zheng, Z. Wang, D. Ma and B. Z. Tang, *Adv. Funct. Mater.*, 2023, **33**, 2212876.

17 K. Jiang, X. Chang, J. Zhu, T. Zhu, J. Yu, Y. Wang, Y. Zhang, D. Ma and W. Zhu, *Angew. Chem., Int. Ed.*, 2025, **64**, e202421520.

18 (*a*) S. Grimme, J. Antony, S. Ehrlich and H. Krieg, *J. Chem. Phys.*, 2010, **132**, 154104; (*b*) S. Grimme, S. Ehrlich and L. Goerigk, *J. Comput. Chem.*, 2011, **32**, 1456.

19 (*a*) P. K. Samanta, D. Kim, V. Coropceanu and J.-L. Brédas, *J. Am. Chem. Soc.*, 2017, **139**, 4042; (*b*) M. K. Etherington, J. Gibson, H. F. Higginbotham, T. J. Penfold and A. P. Monkman, *Nat. Commun.*, 2016, **7**, 13680.

20 Q. Xie, C. Liao, H. Liu, S. Wang and X. Li, *J. Mater. Chem. C*, 2024, **12**, 11085–11093.

21 W. Li, D. Liu, F. Shen, D. Ma, Z. Wang, T. Feng, Y. Xu, B. Yang and Y. Ma, *Adv. Funct. Mater.*, 2012, **22**, 2797.

22 Z. R. Grabowski, K. Rotkiewicz and W. Rettig, *Chem. Rev.*, 2003, **103**, 3899–4032.

23 C. Li, R. Duan, B. Liang, G. Han, S. Wang, K. Ye, Y. Liu, Y. Yi and Y. Wang, *Angew. Chem., Int. Ed.*, 2017, **129**, 11683.

24 (*a*) Q. Zhang, J. Li, K. Shizu, S. Huang, S. Hirata, H. Miyazaki and C. Adachi, *J. Am. Chem. Soc.*, 2012, **134**, 14706; (*b*) Q. Zhang, B. Li, S. Huang, H. Nomura, H. Tanaka and C. Adachi, *Nat. Photon.*, 2014, **8**, 326; (*c*) M. Kim, S. K. Jeon, S.-H. Hwang and J. Y. Lee, *Adv. Mater.*, 2015, **27**, 2515.

25 X. Zhang, H. Dai, Z. Ma, H. Deng, Z. Yang, J. Zhao and Z. Chi, *Chem. Eng. J.*, 2025, **524**, 169158.

26 (*a*) G. Li, B. Li, H. Zhang, X. Guo, C. Lin, K. Chen, Z. Wang, D. Ma and B. Z. Tang, *ACS Appl. Mater. Interfaces*, 2022, **14**, 10627; (*b*) D. Xie, Z. Wang, Y. Chen, X. Qiao, D. Yang, Q. Sun, Y. Dai, Y. Ma and D. Ma, *Adv. Opt. Mater.*, 2024, **12**, 2400561.

27 (*a*) H. Jiang, J. Jin and W.-Y. Wong, *Adv. Funct. Mater.*, 2023, **33**, 2306880; (*b*) X.-C. Fan, K. Wang, Y.-Z. Shi, Y.-C. Cheng, Y.-T. Lee, J. Yu, X.-K. Chen, C. Adachi and X.-H. Zhang,

Nat. Photonics, 2023, **17**, 280; (*c*) H. Wang, Y.-C. Cheng, X.-C. Fan, D.-Y. Chen, X. Xiong, X.-Y. Hao, Y.-Z. Shi, J. Yu, D. Huang, J.-X. Chen, K. Wang and X.-H. Zhang, *Sci. Bull.*, 2024, **69**, 2983.

28 M. A. Baldo, D. F. O'Brien, M. E. Thompson and S. R. Forrest, *Phys. Rev. B*, 1999, **60**, 14422–14428.

29 (*a*) S. Y. Kim and J. J. Kim, *Org. Electron.*, 2010, **11**, 1010; (*b*) S.-Y. Kim, W.-I. Jeong, C. Mayr, Y.-S. Park, K.-H. Kim, J.-H. Lee, C.-K. Moon, W. Brütting and J.-J. Kim, *Adv. Funct. Mater.*, 2013, **23**, 3896.

30 J. R. Sheats, H. Antoniadis, M. Hueschen, W. Leonard, J. Miller, R. Moon, D. Roitman and A. Stocking, *Science*, 1996, **273**, 884–888.